Acta Oceanol. Sin., 2019, Vol. 38, No. 9, P. 12–23
https://doi.org/10.1007/s13131-019-1473-1
http://www.hyxb.org.cn
E-mail: hyxbe@263.net

Modal structure and propagation of internal tides in the northeastern South China Sea

Qian Liu[1, 3], Xiaohui Xie[2], Xiaodong Shang[3]*, Guiying Chen[3], Hong Wang[1]

[1] School of Naval Architecture and Ocean Engineering, Jiangsu University of Science and Technology, Zhenjiang 212003, China

[2] State Key Laboratory of Satellite Ocean Environment Dynamics, Second Institute of Oceanography, Ministry of Natural Resources, Hangzhou 310012, China

[3] State Key Laboratory of Tropical Oceanography, South China Sea Institute of Oceanology, Chinese Academy of Sciences, Guangzhou 510301, China

Received 21 August 2018; accepted 27 September 2018

Abstract

The evolution of energy, energy flux and modal structure of the internal tides (ITs) in the northeastern South China Sea is examined using the measurements at two moorings along a cross-slope section from the deep continental slope to the shallow continental shelf. The energy of both diurnal and semidiurnal ITs clearly shows a ~14-day spring-neap cycle, but their phases lag that of barotropic tides, indicating that ITs are not generated on the continental slope. Observations of internal tidal energy flux suggest that they may be generated at the Luzon Strait and propagate west-northwest to the continental slope in the northwestern SCS. Because the continental slope is critical-supercritical with respect to diurnal ITs, about 4.6 kJ/m^2 of the incident energy and 8.7 kW/m of energy flux of diurnal ITs are reduced from the continental slope to the continental shelf. In contrast, the semidiurnal internal tides enter the shelf because of the sub-critical topography with respect to semidiurnal ITs. From the continental slope to the shelf, the vertical structure of diurnal ITs shows significant variation, with dominant Mode 1 on the deep slope and dominant higher modes on the shelf. On the contrary, the vertical structure of the semidiurnal ITs is stable, with dominant Mode 1.

Key words: South China Sea, internal tides, propagation, scattering, modal structure

Citation: Liu Qian, Xie Xiaohui, Shang Xiaodong, Chen Guiying, Wang Hong. 2019. Modal structure and propagation of internal tides in the northeastern South China Sea. Acta Oceanologica Sinica, 38(9): 12–23, doi: 10.1007/s13131-019-1473-1

1 Introduction

Internal tides (ITs), internal gravity waves at or near tidal frequencies, are ubiquitous in stratified waters where they are generated in response to tidal flows that are incident upon bottom topography, such as subsurface ridges, seamounts and the continental shelf slope (Egbert and Erofeeva, 2002; Garrett and Kunze, 2007). Internal tides generated on the continental slope are characterized by high spatial and temporal variability and propagate both upslope towards the coast and downslope towards deeper water (Pingree and New, 1991). Internal tides are believed to significantly contribute to underwater sound propagation (Powell et al., 2013), regional ecosystems (Jan and Chen, 2009), abyssal mixing and overturning circulation (Munk and Wunsch, 1998).

The South China Sea (SCS) is part of a chain of marginal seas along the western Pacific Ocean and connected by a number of straits with varying width and depth. The most important one is the Luzon Strait located between Taiwan and the Island of Luzon in the Philippines, connecting the SCS to the western Pacific Ocean. Due to the steep submarine ridges and strong barotropic tidal currents, the Luzon Strait is one of the most energetic barotropic to baroclinic conversion sites in the world's oceans (Niwa and Hibiya, 2004; Xu et al., 2016). As one of the most energetic internal tide generation site in the global oceans, the Luzon Strait radiates internal tides both westward into the SCS basin and eastward into the western Pacific (Zhao, 2014; Xu et al., 2016). Dissipation of these energetic ITs provide energy for turbulent mixing in the deep SCS (Tian et al., 2009), driving deep-water circulation (Zhao et al., 2014). When the energetic internal tides propagate westward from Luzon Strait to the continental slope in the northern SCS, they may lose their energy in different behaviors. Using mooring data collected at a deep site on the continental slope on the east side of Dongsha Island, Klymak et al. (2011) suggested that diurnal internal tides may scatter into higher modes and lead to strong bottom dissipation due to the effects of near-critical reflection on the slope. Xie et al. (2018) confirmed strong near-bottom dissipation of diurnal internal tides on the slope and suggested that strong internal tidal dissipation may lead to generation of along-slope bottom circulation in the northern SCS. Semidiurnal internal tides, on the other hand, can lose their energy via disintegrating into large-amplitude internal solitary waves (Zhao et al., 2014; Lien et al., 2005; Farmer et al., 2009). Using a set of

Foundation item: The State Key Laboratory of Tropical Oceanography, South China Sea Institute of Oceanology, Chinese Academy of Sciences under contract No. LTO1915; the National Natural Science Foundation of China under contract Nos 41630970, 41876016, 41676022 and 41521005; the Instrument Developing Project of the CAS under contract No. YZ201432.
*Corresponding author, E-mail: xdshang@scsio.ac.cn

mooring current record, Xie et al. (2013) suggested that near-surface reflection of semidiurnal internal tides on the continual slope may enhance nonlinear stability which transfers energy of semidiurnal internal tides to mean flows, nonlinear sub-harmonics and super-harmonics.

Because of the topographic effects, one may expect significant variations of internal tides from the continual slope to shelf. However, observations showing variation of internal tidal vertical structure and energy flux direction, as they propagate from the deep continental slope (>1 000 m) to the continental shelf, have been rarely reported. Duda and Rainville (2008) analyzed multiple sets of mooring data in a cross-slope line near Donsha Island and showed that internal tidal energy flux on the continental slope and shelf has a large difference. However, their observations were confined to the shallow portion of the continental slope. Furthermore, the evolution of wave structure is not investigated. In an attempt to address this issue, a field program was implemented in the northern SCS to obtain detailed observations of the ITs over a cross-slope section from the deep slope to the shallow shelf. The mooring positions were in a line moving up from the deep continental slope to the shallow continental shelf, in a water depth range between 1 249 and 275 m. The aim of this work is to investigate the evolution of the energy flux and modal structure of ITs as they propagate shoreward from deep water to the shallow shelf.

This paper is organized as follows. The experimental area, the moored instrumentation, data and analysis methods are introduced in Section 2. Section 3 presents the qualitative and quantitative picture of the ITs from the slope to the shelf. Section 4 discusses the possible reasons leading to internal tidal variation, and the conclusions are presented in Section 5.

2 Methodology

2.1 *Moorings*

Mooring current, temperature, and conductivity data were collected during the summer months (August–September) of 2014 in the northeastern SCS (Fig. 1), when the ITs are stronger (Shang et al., 2015; Xu et al., 2014). Along a cross-slope section, two mooring instruments were deployed at two fixed sites: A and B (Fig. 1). The Site A was located on the continental slope, and B was located on the shelf. Figure 1 shows the detailed mooring locations. The water depths at the Sites A and B were 1 249 and 275 m, respectively.

The current records at Site A were obtained from three ADCPs: one upward-looking WHS75K ADCP moored near 440-m deep (effective data from 84 m to 420 m); one downward-looking WHS75K ADCP moored near 450-m deep (effective data from 478 m to 942 m); and another downward-looking WHS150K ADCP moored near 950-m deep (effective data from 972 m to 1 116 m). At this mooring site, temperature data were measured using different instruments, including two Seabird conductivity temperature depths (CTDs) and 15 Seabird Temperature loggers. Detailed information on mooring data is given in Table 1. The current data covered more than 80% of the water depth, whereas the temperature data covered more than 90%.

The shelf Mooring B consisted of a single upward-looking WHS150K ADCP that was placed on the seafloor and a thermistor chain with nine sensors at depths of 57, 67, 87, 107, 147 and 187 m. The upward-looking ADCP provided current measurements every 8-m from 33 m to 241 m, at a water depth of 275 m.

2.2 *Band-pass filtering*

The diurnal and semidiurnal components in raw current and temperature time series at two mooring sites are extracted by a band-pass filtered technique based on a second-order Butterworth filter. Cutoff frequencies of the diurnal band, centered at O_1 and K_1 tidal frequencies, are set to [0.85, 1.15] cpd. Cutoff frequencies of [1.7, 2.3] cpd are used to extract the semidiurnal components.

2.3 *Harmonic analysis of the internal tides*

The barotropic currents at each mooring are defined as the depth-averaged currents. The baroclinic currents are computed as the raw current deduction of the depth-averaged value. To document the spatial structure of the primary tidal constituents,

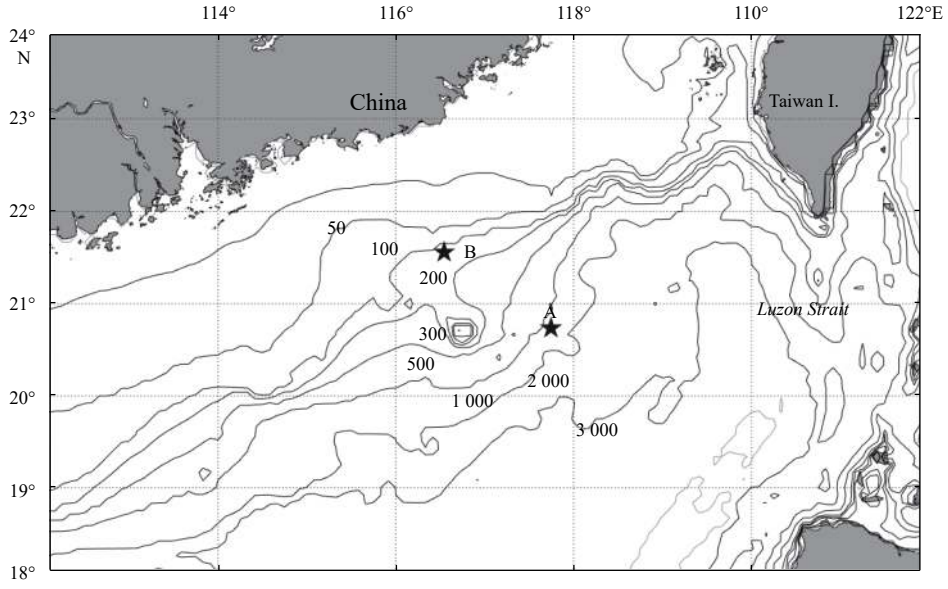

Fig. 1. Bathymetry and the mooring sites (black star) in the northern South China Sea.

Table 1. Mooring information and instrument configurations

Mooring	Location	Depth/m	Sampling interval/min	Vertical resolution/m	Time range (yearday)
Site A	20°44.2′N, 117°44.7′E	1 249			
	upward-looking 75-kHz ADCP	84–420	2	16	212.5–267
	downward-looking75-kHz ADCP	478–942	2	16	212.5–267
	downward-looking150-kHz ADCP	972–1 116	1.5	8	212.5–267
	thermistor chain	50–1 235	1/6	20, 50	212.5–267
Site B	21°33.48′N, 116°32.6′E	275			
	upward-looking 150-kHz ADCP	33–241	1.5	8	212.5–268
	thermistor chain	60–190	1/6	10, 20	212.5–268

tidal harmonic analysis is performed on horizontal currents at each observational depth.

2.4 *Vertical displacement*

Vertical displacement is calculated from temperature measurements at each mooring.

$$\eta(z,t) = \left[T(z,t) - \overline{T}(z,t)\right] / T_z(z,t), \tag{1}$$

where $T(z,t)$ is the temperature as a function of depth (z) and time (t), $\overline{T}(z,t)$ is the time-averaged temperature and $T_z(z,t)$ is the vertical temperature gradient (Zhao et al., 2010).

2.5 *Modal decomposition*

In an ocean with water depth H, the baroclinic modes for the vertical displacement $\Phi(z)$ and the horizontal velocity$\Pi(z)$, with the boundary conditions $\Phi(0)$ =$\Phi(H)$ =0, can be determined by the following Taylor-Goldstein equations:

$$\frac{\mathrm{d}^2\Phi(z)}{\mathrm{d}z^2} + \frac{N^2(z)}{C_n^2}\Phi(z) = 0, \tag{2}$$

and

$$\Pi(z) = \rho_0 {C_n}^2 \frac{\mathrm{d}\Phi(z)}{\mathrm{d}z}, \tag{3}$$

where ρ_0 is the water density, C_n is the eigenspeed (Gill, 1982), and n is the mode number. The observed internal tides at two mooring sites are dominated by lower modes, which will be shown in Section 3.3. Therefore, only the first three baroclinic modes are extracted in modal decomposition.

The baroclinic velocity and displacement are expressed as

$$u'(z,t) = \sum_{n=1}^{3} {u'}_n(t)\,\Phi_n(z), \tag{4}$$

and

$$\eta'(z,t) = \sum_{n=1}^{3} {\eta'}_n(t)\,\Pi_n(z), \tag{5}$$

where ${u'}_n(t)$ and ${\eta'}_n(t)$ stand for the time-varying magnitudes of the baroclinic modes (Zhao et al., 2010; Alford, 2003), and $\Phi_n(z)$ and $\Pi_n(z)$ are the vertical structures of the baroclinic modes. Additionally, ${u'}_n(t)$ and ${\eta'}_n(t)$ can be extracted from the velocity and displacement profiles by least-squares modal fitting (Nash et al., 2005). At each mooring site, the buoyancy frequency $N(z)$ computed from a Yoyo-CTD profile, which was performed near the mooring site during the mooring period, is used to calculate the modal function (Fig. 2). Our water column coverage is sufficient to compute the first three baroclinic modes (Nash et al., 2005).

Depth-integrated horizontal kinetic energy (HKE) and available potential energy (APE) are then computed from the above modal fit baroclinic perturbations, $u'(z,t)$ and $\eta'(z,t)$, by

$$\mathrm{HKE} = \int_{-H}^{0} \left\langle \frac{1}{2}\rho_0 \left|u'(z,t)\right|^2 \right\rangle \mathrm{d}z \tag{6}$$

and

$$\mathrm{APE} = \int_{-H}^{0} \left\langle \frac{1}{2}\rho_0 N^2(z)\,{\eta'}^2(z,t) \right\rangle \mathrm{d}z, \tag{7}$$

where the angle brackets indicate an average over one tidal cycle. The total energy (E) is calculated by

$$E = \mathrm{HKE} + \mathrm{APE}. \tag{8}$$

The depth-integrated energy flux (Flux, F) is computed as the covariance of the modal fit velocity $u'(z,t)$ and pressure perturbation $P'(z,t)$ by

$$F = \int_{-H}^{0} \langle u'(z,t)\,P'(z,t)\rangle \,\mathrm{d}z, \tag{9}$$

$$P'(z,t) = \rho_0 \int_{-z}^{0} N^2(z,t)\,\eta'(z,t)\,\mathrm{d}z - P_{\mathrm{surf}}(t). \tag{10}$$

The definition of baroclinic motion requires the depth average of the baroclinic pressure perturbation to be zero; hence, the surface baroclinic pressure $P_{\mathrm{surf}}(t)$ is computed as follows:

$$P_{\mathrm{surf}}(t) = \frac{1}{H}\rho_0 \int_{-H}^{0} N^2(z,t)\,\eta'(z,t)\,\mathrm{d}z. \tag{11}$$

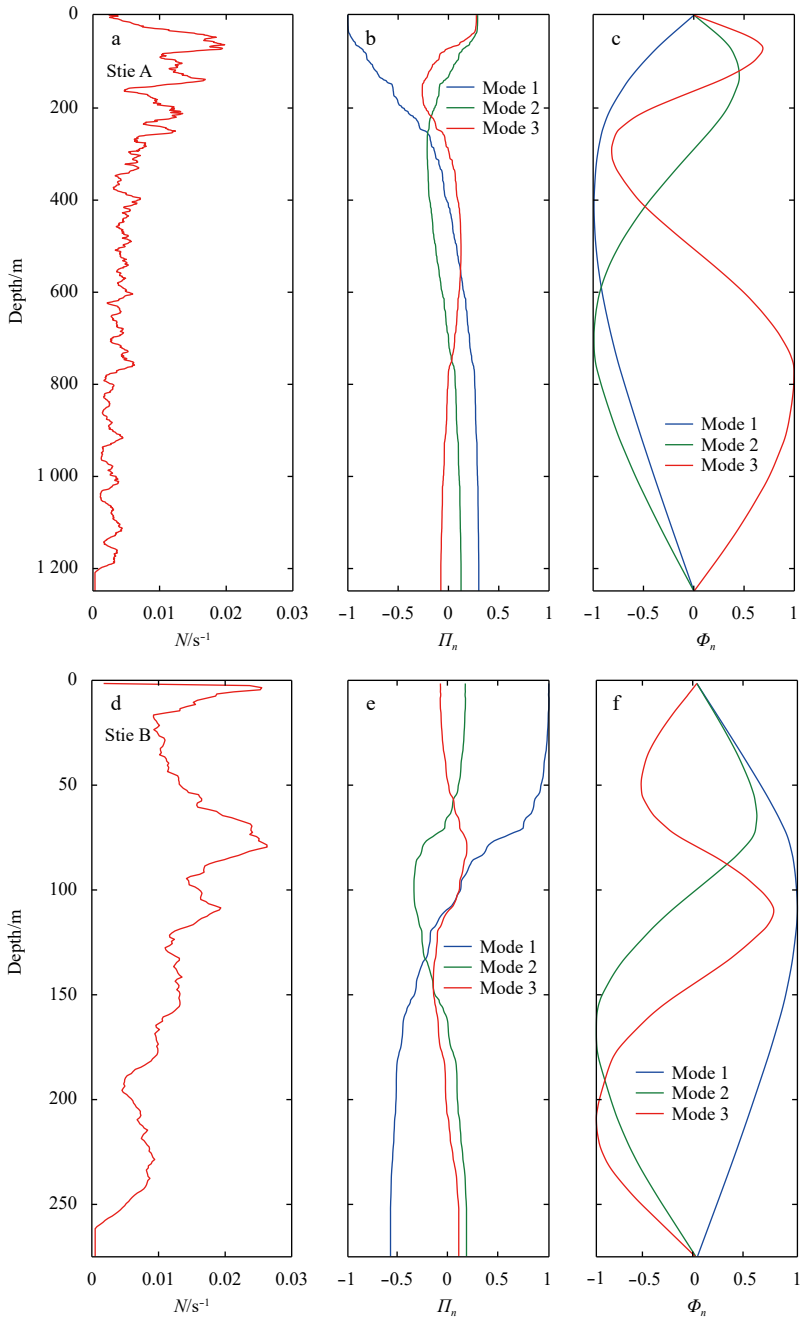

Fig. 2. Buoyancy frequency profiles of Site A (a) and Site B (d). Normalized vertical structures of the first three baroclinic modes for horizontal velocity of Site A (b) and Site B (e) and vertical displacement of Site A (c) and Site B (f).

3 Results

3.1 *Raw and baroclinic currents*

Before proceeding to more quantitative analyses, a linear interpolation was made to replace some rare, unrealistic extreme values in the raw data. A 4-day sample of the raw east-west velocities and isotherms at two mooring sites is shown in Fig. 3. Both moorings show strong baroclinic tidal signals and high frequency internal solitary waves, which were previously observed near Dongsha Island (Duda et al., 2004; Klymak et al., 2011). Internal tidal signals have pronounced downward (upward) phase (energy) propagation, implying a multimode vertical structure rather than a single mode response at Site A.

These strong baroclinic tidal motions, as well as their upward energy propagation, can be more clearly identified in the band-pass filtered diurnal and semidiurnal velocities (Fig. 4). It is also shown that there are stronger diurnal motions at Site A, but diurnal and semidiurnal signals have comparable amplitudes at Site B.

3.2 *Harmonic analysis of baroclinic tidal currents*

To investigate the variance of the amplitude and phase of several primary internal tidal constituents at two moorings, harmonic analysis is performed on the time series of the baroclinic cur-

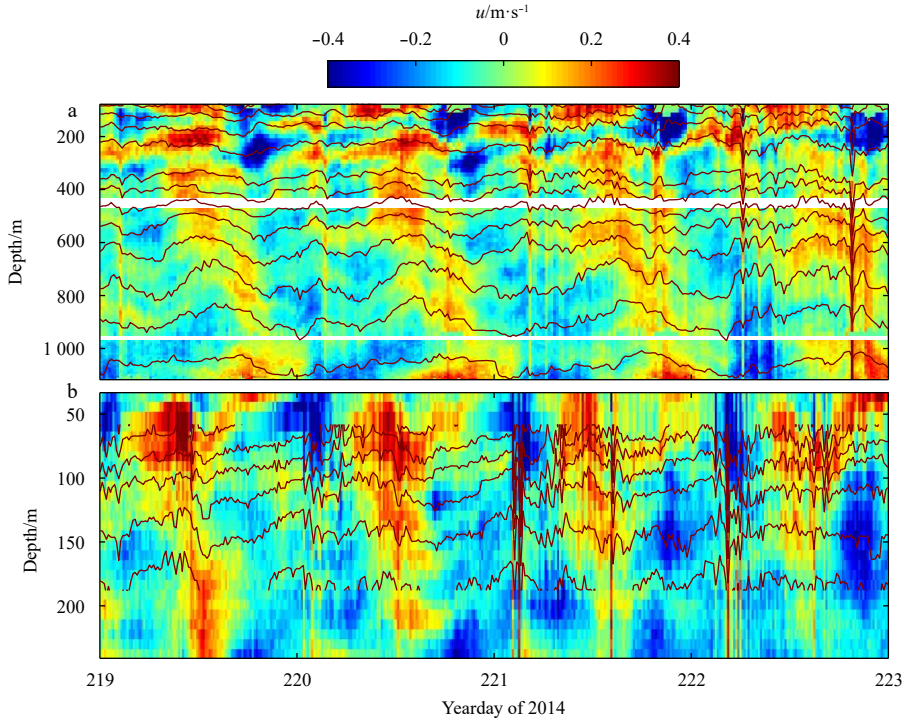

Fig. 3. A 4-day segment of the zonal (east–west) velocities and isotherms at the corresponding site. a. Site A and b. Site B.

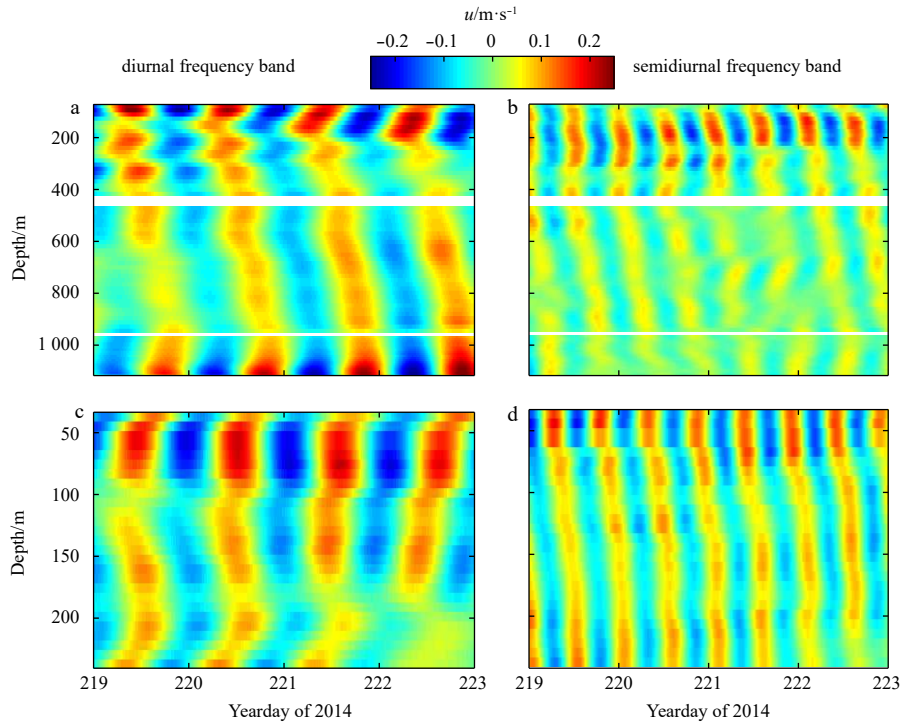

Fig. 4. Band-pass filtered diurnal (left) and semidiurnal (right) signals at two sites. a and b. Site A, and c and d. Site B.

rent at each depth. Four (O_1, K_1, M_2, S_2) primary internal tidal ellipses at two mooring sites are shown in Fig. 5. Diurnal O_1 and K_1 constituents show a clear decrease from the deep slope (Site A) to the shelf (Site B), whereas the semidiurnal M_2 component is still strong on the shelf. The orientations of M_2, K_1 and O_1 constituents are approximately northwest-southeast. In contrast, O_1 and K_1 on the shelf show the presence of higher mode motions and their ellipse major axes have large depth variation. For the semidiurnal M_2 and S_2 components, their current ellipses are mainly oriented in the east-west direction at Site A, whereas they are oriented in the northwest-southeast direction at Site B. At most depths, the elliptical polarization of the four primary baroclinic components at two moorings is rotated significantly clockwise, which is consistent with that of freely propagating waves in the

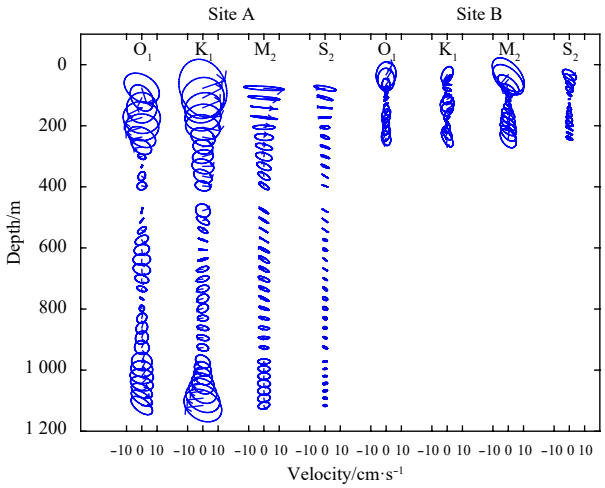

Fig. 5. Vertical structures of O_1, K_1, M_2 and S_2 baroclinic tidal ellipse of two sites. The ellipses are centred at their corresponding measurement depths. The arrows denote the rotation directions of ellipses, and the lines from the centre show the Greenwich phases.

northern hemisphere (van Haren, 2005; Xie et al., 2010; Liu et al., 2016).

3.3 *Temporal and spatial structure of energy and flux*

3.3.1 *Diurnal ITs*

At Site A, a 14-day spring-neap cycle is clearly visible in terms of both diurnal velocity and displacement (Figs 6a–c). The cycles in the velocity and the displacement have the same phase. Spring tide signals are visually greatest near the surface and bottom with respect to velocity (Figs 6a and b), although the displacement is greatest in the middle of the water column (Fig. 6c). This is consistent with a primarily mode-1 signal. Furthermore, the currents in the shallow and deep water demonstrate opposite phases, with minimum velocity approaching the mode-1 node near 400 m (refer to Fig. 2b). This observation confirms the dominance of mode-1 diurnal ITs (Figs 6a and b).

The total depth-integrated energy (Figs 6d–f) and flux magnitude (Fig. 6g) show the clear 14-day spring-neap cycle and the dominant Mode 1, except for the available potential energy, with a greater Mode 2 signal. Mode 1 signals at this site account for 68% of the total energy and 67% of the energy flux (Table 2). To examine whether the ITs are generated near the continental slope, time series of the corresponding barotropic current magnitudes at diurnal bands are also plotted (Fig. 6h). A primarily fortnightly temporal pattern of the diurnal barotropic current can be clearly identified, but its phase is ~2 days earlier than that of the diurnal ITs, implying that the diurnal ITs are not locally generated.

Compared with diurnal ITs at Site A, diurnal ITs on the continental shelf (Mooring B) are relatively complicated (Fig. 7). Their energy and flux are significantly reduced, indicating large energy dissipation from the deep slope to the continental shelf. Furthermore, the 14-day cycle is ambiguous. The phase of HKE is asynchronous with APE (Fig.7e) at this site (Figs 7d–e). Mode 1, Mode 2 and Mode 3 signals at this site account for 42%, 34% and 23% of the total energy, respectively (Fig. 7d), and the dominance of Mode 1 and Mode 2 for APE (Fig. 7e) and Flux (Fig. 7g). The lag time between two neighboring maximums of the diurnal internal tidal energy and barotropic current magnitude is nearly 4 days (Figs 7f–h).

3.3.2 *Semidiurnal ITs*

The time lags between semidiurnal ITs and barotropic forcing also exist at two sites. At Site A, the semidiurnal internal tides are dominated by Mode 1 (Figs 8a–g). Their APE is greater than HKE (Figs 8d and e). The semidiurnal 14-day spring-neap cycle for displacement is visible but it is ambiguous in the velocity field.

The dominance of Mode 1 semidiurnal ITs also occurs at Mooring B (Figs 9a–g). The Mode 1 signals contain more than 95% of the flux and 90% of the energy (Table 2). The semidiurnal 14-day cycle is visible for both velocity/HKE and displacement/APE.

3.4 *Direction of energy flux*

Based on Section 3.3, it was suggested that the ITs are not locally generated at two sites. To further study the propagation of ITs, we compare the energy flux vectors of ITs for diurnal and semidiurnal bands at two observational sites. Figures 10 and 11 show the time series of baroclinic energy flux vectors at Site A and Site B.

The diurnal energy flux vector at Site A is directed across the isobaths on the northern slope and is nearly in alignment with the mooring line (Fig. 10a). This suggests that the net flux of diurnal internal tides is northwestward. The flux direction does not represent the true propagation direction of waves because diurnal internal tides may be reflected on the continental slope in the northern SCS (Klymak et al., 2011). The wave reflection and interference may lead to confusing patterns of wave kinematics (propagation directon) and energy fluxes (Rainville et al., 2010; Zhao et al., 2010). The flux vector of diurnal ITs at Site B shows that the northward net flux is dominant (Fig. 11a). Based on the energy flux direction on the slope, we deduce that observed ITs should be mainly generated at the Luzon Strait, as previously reported in most studies on internal tides near Dongsha Island (e.g., Duda et al., 2004; Duda and Rainville, 2008).

For semidiurnal ITs, the energy flux vector at Site A is directed nearly due west, namely, toward Dongsha Island (Fig. 10b). This is slightly different from the diurnal ITs with the net flux vector pointing toward the northwestern continental shelf at this site. The direction of the time-average flux is approximately 165° from due east, which is consistent with the satellite altimetric results in Zhao (2014). Huang et al. (2018) showed that the mesoscale eddies may modulate the propagation direction of the semidiurnal internal tides on the continental slope. However, such modulation is not observed because the flux direction does not show a significant difference during the entire observational period. At Site B, the direction of the semidiurnal energy flux (Fig. 11b) is ~120° from due east (northwest), which is slightly different from that (quasi-west) observed on the deep slope.

4 Discussion

In Section 3, it was shown that only 14% of diurnal internal tidal energy is radiated to the shelf; that is, ~4.6 kJ/m^2 horizontal kinetic energy and ~8.7 kW/m energy flux are reduced from the continental slope to continental shelf. In contrast, more than 60% of semidiurnal energy enters the shelf. There are two possible reasons that can explain the large reduction in diurnal internal

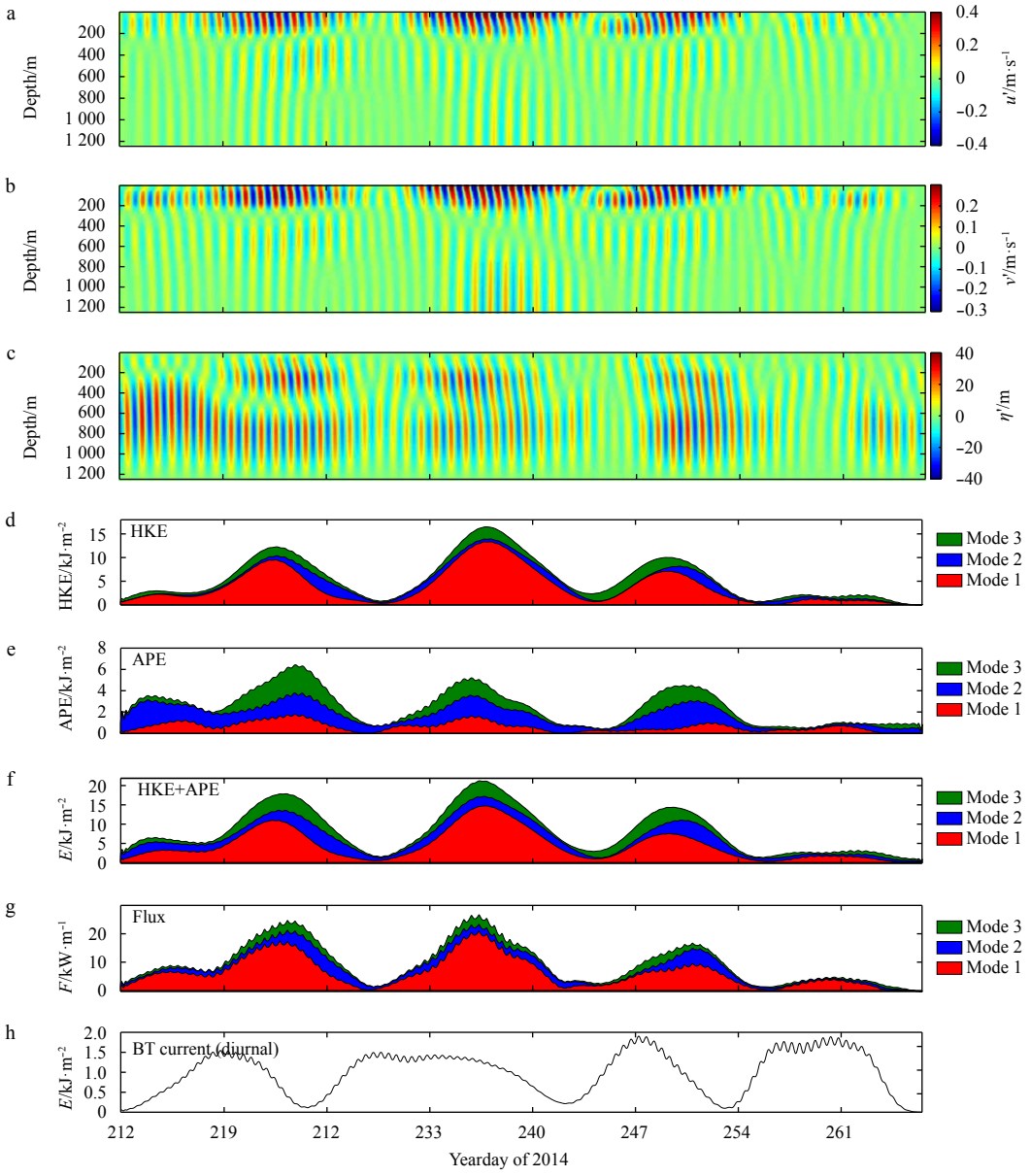

Fig. 6. Diurnal internal tides at Site A. a. Eastward velocity, b. northward velocity, c. vertical displacement, d. HKE, e. APE, f. HKE+APE, g. flux magnitude, and h. barotropic current magnitude at diurnal band.

Table 2. Time-mean modal distribution of diurnal and semidiurnal HKE (kJ/m²), APE (kJ/m²), and Flux (kW/m) at Site A and Site B

Site A		Mode 1	Mode 2	Mode 3	Total
Diurnal	HKE	3.717 9	0.762 4	0.993 6	5.473 9
	APE	0.637 1	1.094 1	0.736 8	2.468 0
	Flux	6.191 0	1.859 9	1.206 5	9.257 4
Semidiurnal	HKE	1.314 1	0.847 3	0.320 9	1.908 6
	APE	1.819 5	0.926 9	0.221 9	2.968 3
	Flux	6.839 7	1.982 5	0.339 3	9.161 5
Site B		Mode 1	Mode 2	Mode 3	Total
Diurnal	HKE	0.331 9	0.264 3	0.181 7	0.777 9
	APE	0.096 9	0.094 2	0.047 2	0.238 3
	Flux	0.347 2	0.147 2	0.050 3	0.544 7
Semidiurnal	HKE	1.032 8	0.080 9	0.025 3	1.139 0
	APE	0.733 0	0.079 8	0.018 3	0.831 1
	Flux	2.212 3	0.077 5	0.011 0	2.300 8

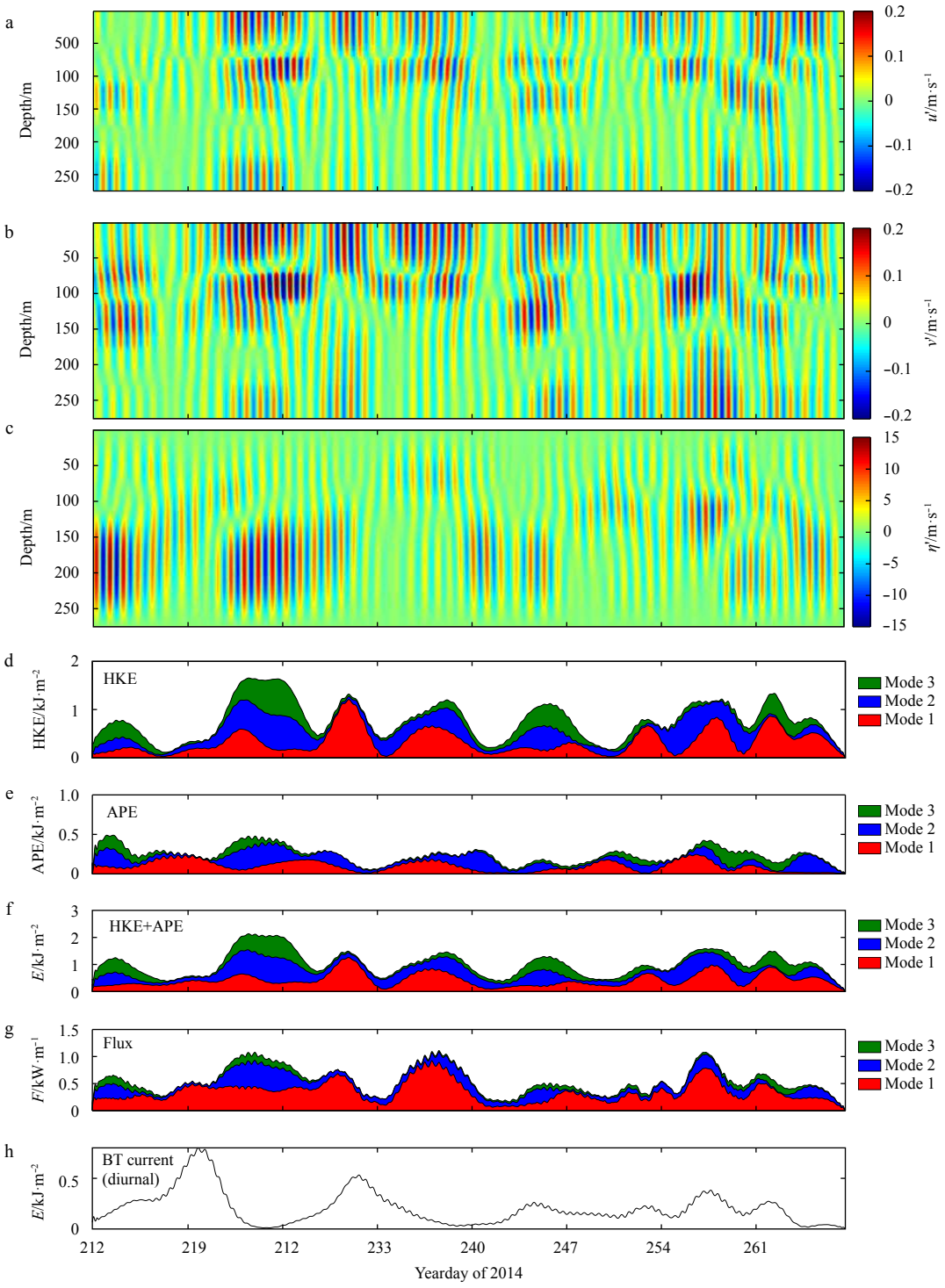

Fig. 7. Diurnal internal tides at Site B. a. Eastward velocity, b. northward velocity, c. vertical displacement, d. HKE, e. APE, f. HKE+APE, g. flux magnitude, and h. barotropic currents magnitude at diurnal band.

tides. On the slope near Dongsha Island, the seafloor inclination is critical-supercritical for diurnal internal waves, while it is subcritical for semidiurnal waves (Duda et al., 2008; Klymak et al., 2011; Xie et al., 2018). Diurnal internal tides, on one hand, may be reflected downslope to the deep water (Klymak et al., 2011; Xie et al., 2018). On the other hand, they may also be scattered into higher modes and significantly dissipate their energy on the slope due to near-critical reflection (Klymak et al., 2011; Xie et al., 2018). Thus, it is not surprising that only a small fraction of diurnal ITs are radiated to the shelf. Because of the reflection, the propagation direction of internal tides may be altered when ITs reach the shallow Mooring B, as shown in Fig. 11. Because of the scattering of low-mode internal tides into higher modes, the vertical structure of diurnal ITs is more complicated when they propagate to the shelf, as shown in Fig. 7.

For semidiurnal internal tides, most of their energy is not re-

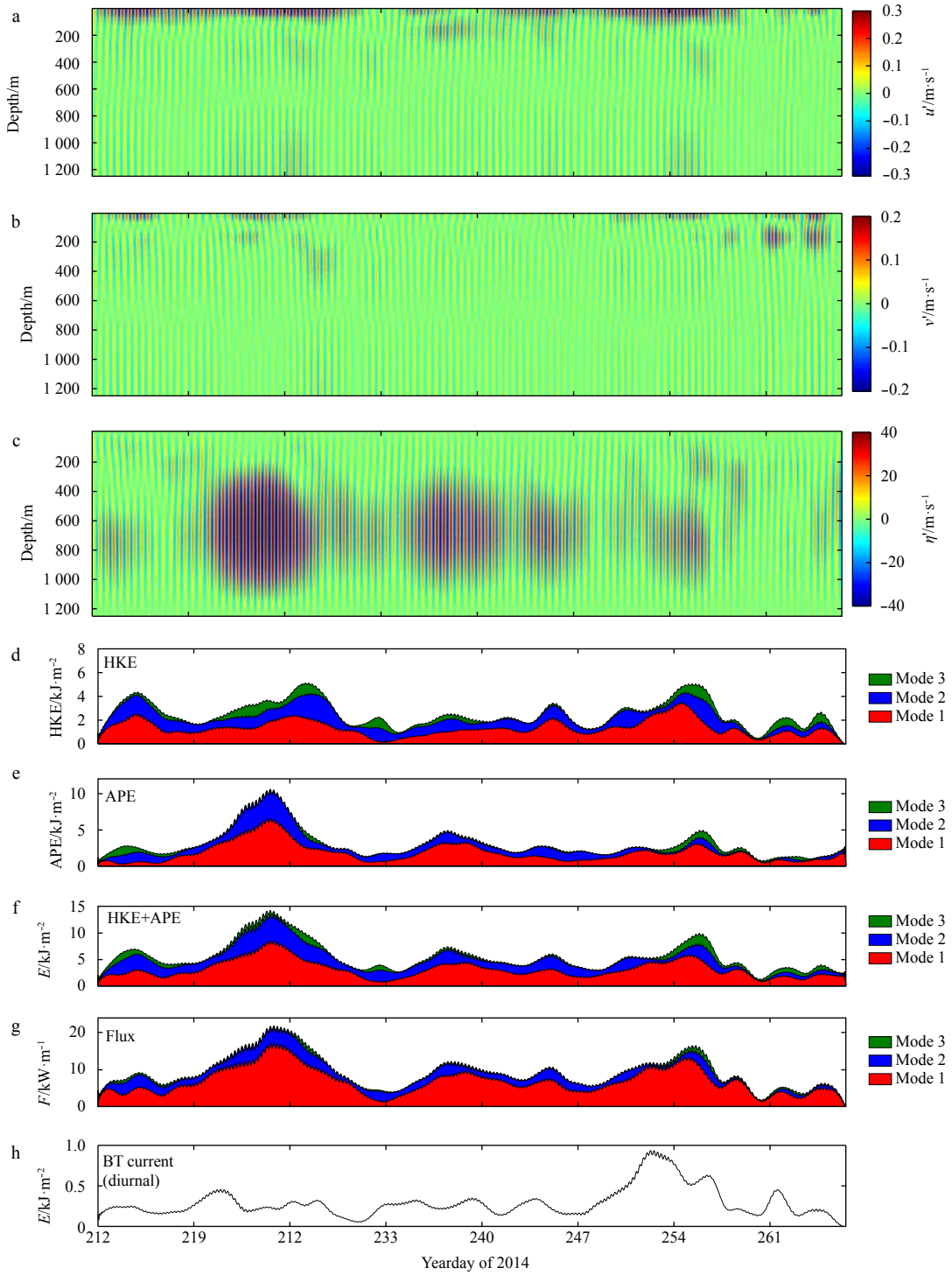

Fig. 8. Semidiurnal internal tides at Site A. a. Eastward velocity, b. northward velocity, c. vertical displacement, d. HKE, e. APE, f. HKE+APE, g. flux magnitude, and h. barotropic currents magnitude at semidiurnal band.

flected or dissipated due to a subcritical topography (Klymak et al., 2011), and more energy can therefore be radiated upslope to the shelf. However, the propagation direction is changed from quasi-west on the slope to northwest on the shelf.

5 Summary and conclusions

Using two sets of mooring records obtained in the northern SCS, this paper documents the evolution of the energy, energy flux and modal structure of ITs at diurnal and semidiurnal bands as they propagate from the deep continental slope to the shallow continental shelf. The phase of the internal tidal energy lags the corresponding barotropic tides at both diurnal and semidiurnal bands. This is consistent with previous studies on internal tides on Dongsha Island, where internal tides are believed to result from the Luzon Strait (Duda et al., 2004; Duda and Rainville, 2008).

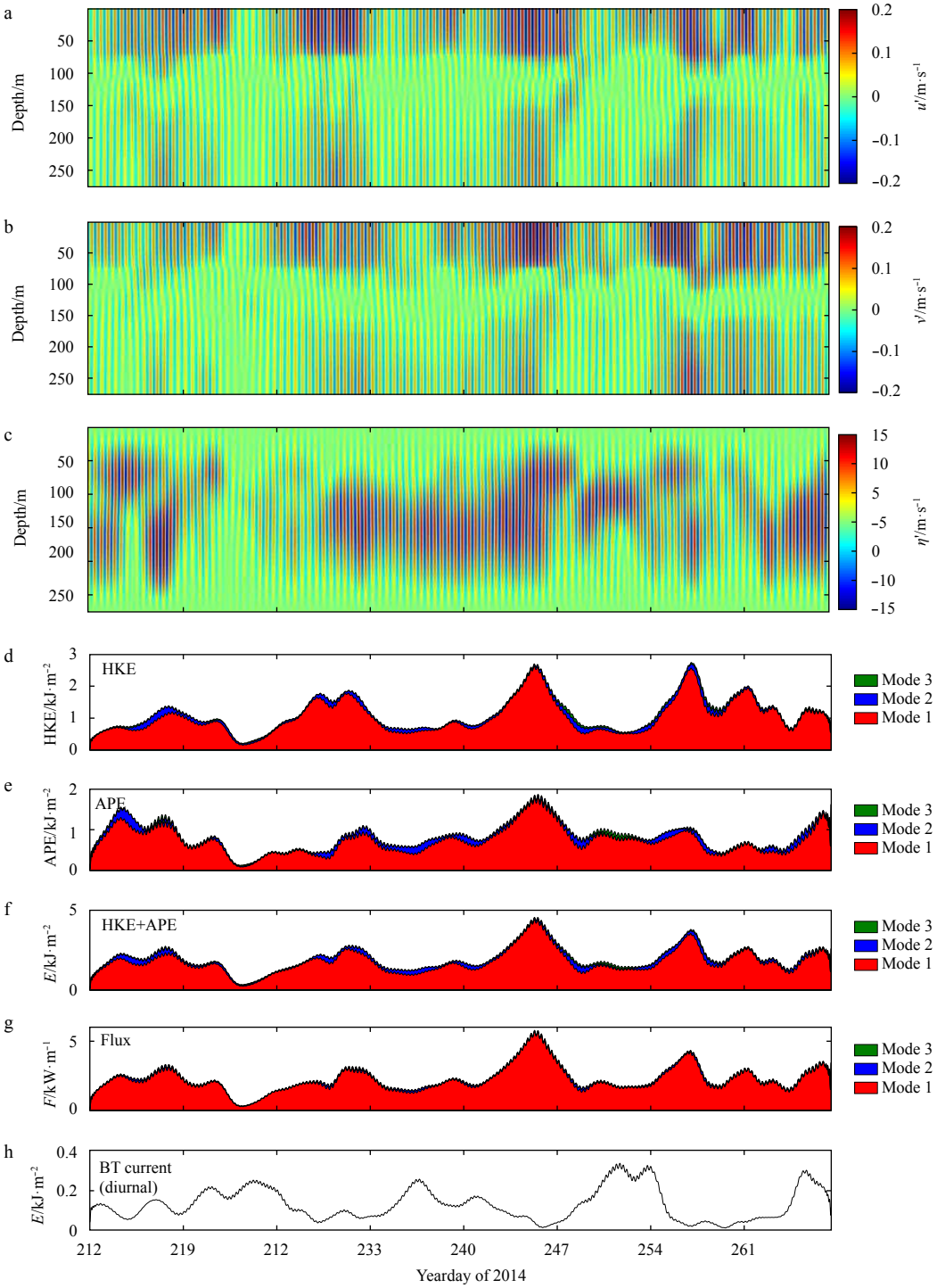

Fig. 9. Semidiurnal internal tides at Site B. a. Eastward velocity, b. northward velocity, c. vertical displacement, d. HKE, e. APE, f. HKE+APE, g. flux magnitude, and h. barotropic currents magnitude at semidiurnal band.

For diurnal ITs, the energy is reduced almost 86% when they propagate upslope to the shelf due to dissipation or reflection under the role of critical-supercritical seafloor inclination. Furthermore, the low-mode diurnal energy may be transferred to a higher mode, with Mode 1 dominating at Mooring A, and the equivalent Mode 1, Mode 2 and Mode 3 at Mooring B (Fig. 12a). Besides, the direction of diurnal ITs time-average energy flux changed from northwest on the continental slope (Site A) to northward on the continental shelf (Site B).

Compared with those observed on the slope, semidiurnal ITs on the shelf still have considerable energy (Fig. 12b) and more than 60% of the energy for semidiurnal ITs is radiated upslope to the shelf due to the subcritical topography. Furthermore, they are dominated by Mode 1 both on the deep slope and the shallow shelf. Although the propagation directions of semidiurnal ITs on the slope and shelf are slightly different, they propagate across local isobaths and toward the shallow coast.

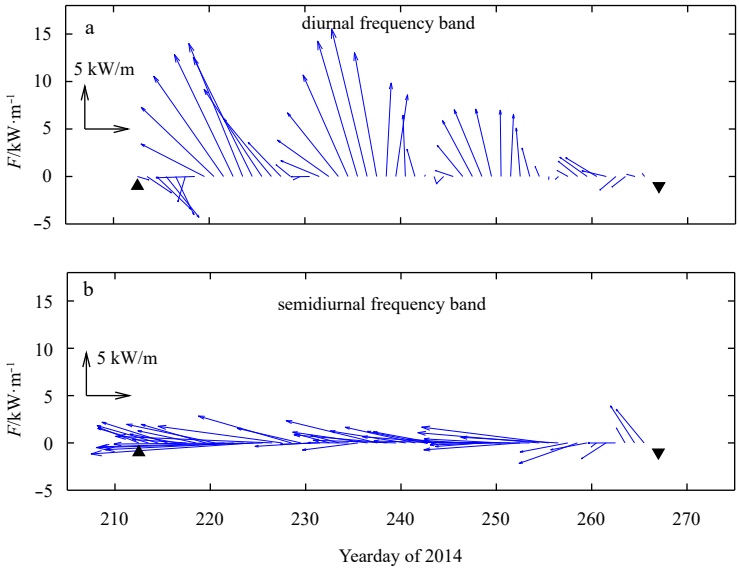

Fig. 10. Time series of energy flux for diurnal (a) and semidiurnal (b) species at mooring Site A. The up and down triangles indicate the start and end, respectively, of each time series.

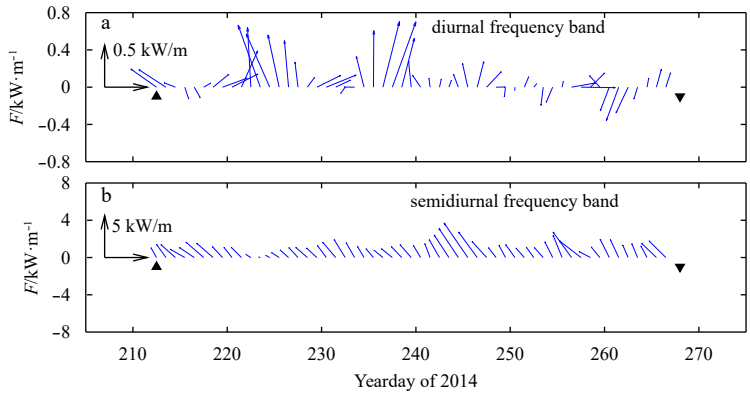

Fig. 11. Time series of energy flux for diurnal (a) and semidiurnal (b) species at mooring Site B. The up and down triangles indicate the start and end, respectively, of each time series.

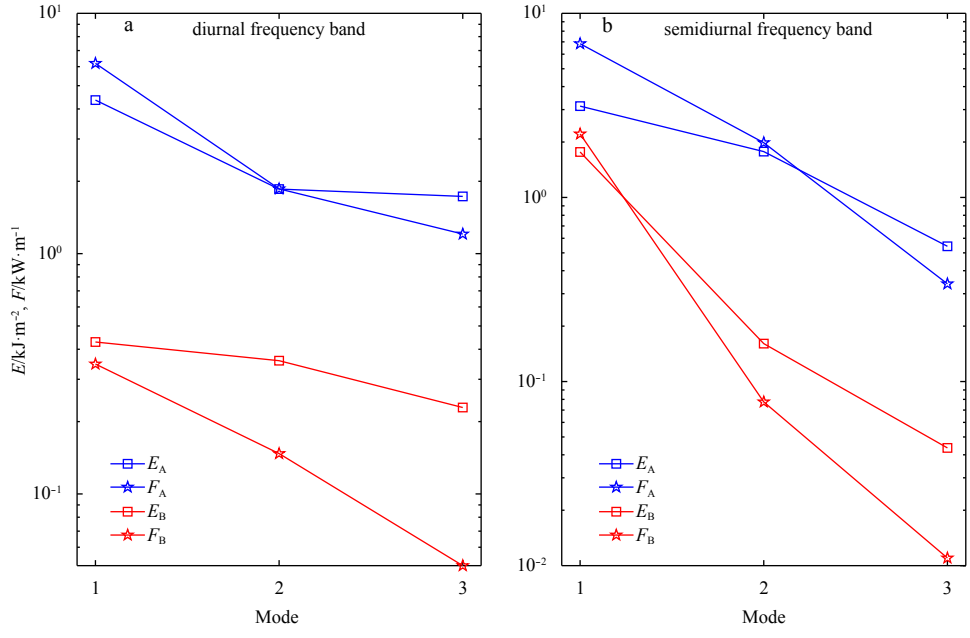

Fig. 12. Time-mean modal distribution of the diurnal (a) and semidiurnal (b) total energy and energy flux at Sites A and B.

References

Alford M H. 2003. Redistribution of energy available for ocean mixing by long-range propagation of internal waves. Nature, 423(6936): 159–162, doi: 10.1038/nature01628

Duda T F, Lynch J F, Irish J D, et al. 2004. Internal tide and nonlinear internal wave behavior at the continental slope in the northern South China Sea. IEEE Journal of Oceanic Engineering, 29(4): 1105–1130, doi: 10.1109/JOE.2004.836998

Duda T F, Rainville L. 2008. Diurnal and semidiurnal internal tide energy flux at a continental slope in the South China Sea. Journal of Geophysical Research: Oceans, 113(C3): C03025

Egbert G D, Erofeeva S Y. 2002. Efficient inverse modeling of Barotropic ocean tides. Journal of Atmospheric and Oceanic Technology, 19(2): 183–204, doi: 10.1175/1520-0426(2002)019<0183:EIMOBO>2.0.CO;2

Farmer D, Li Q, Park J H. 2009. Internal wave observations in the South China Sea: The role of rotation and non-linearity. Atmosphere-Ocean, 47(4): 267–280, doi: 10.3137/OC313.2009

Garrett C, Kunze E. 2007. Internal tide generation in the deep ocean. Annual Review of Fluid Mechanics, 39: 57–87, doi: 10.1146/annurev.fluid.39.050905.110227

Gill A E. 1982. Atmosphere-Ocean Dynamics. New York: Academic Press

Huang X D, Wang Z Y, Zhang Z W, et al. 2018. Role of mesoscale eddies in modulating the semidiurnal internal tide: observation results in the northern South China Sea. Journal of Physical Oceanography, 48(8): 1749–1770, doi: 10.1175/JPO-D-17-0209.1

Jan S, Chen C T A. 2009. Potential biogeochemical effects from vigorous internal tides generated in Luzon Strait: A case study at the southernmost coast of Taiwan. Journal of Geophysical Research: Oceans, 114(C4): C04021

Klymak J M, Alford M H, Pinkel R, et al. 2011. The breaking and scattering of the internal tide on a continental slope. Journal of Physical Oceanography, 41(5): 926–945, doi: 10.1175/2010JPO4500.1

Lien R C, Tang T Y, Chang M H, et al. 2005. Energy of nonlinear internal waves in the South China Sea. Geophysical Research Letters, 32(5): L05615

Liu Qian, Xie Xiaohui, Shang Xiaodong, et al. 2016. Coherent and incoherent internal tides in the southern South China Sea. Chinese Journal of Oceanology and Limnology, 34(6): 1374–1382, doi: 10.1007/s00343-016-5171-5

Munk W, Wunsch C. 1998. Abyssal recipes II: Energetics of tidal and wind mixing. Deep Sea Research Part I: Oceanographic Research Papers, 45(12): 1977–2010, doi: 10.1016/S0967-0637(98)00070-3

Nash J D, Alford M H, Kunze E. 2005. Estimating internal wave energy fluxes in the ocean. Journal of Atmospheric and Oceanic Technology, 22(10): 1551–1570, doi: 10.1175/JTECH1784.1

Niwa Y, Hibiya T. 2004. Three-dimensional numerical simulation of M2 internal tides in the East China Sea. Journal of Geophysical Research: Oceans, 109(C4): C04027

Pingree R D, New A L. 1991. Abyssal penetration and bottom reflection of internal tidal energy in the Bay of Biscay. Journal of Physical Oceanography, 21(1): 28–39, doi: 10.1175/1520-0485(1991)021<0028:APABRO>2.0.CO;2

Powell B S, Kerry C G, Cornuelle B D. 2013. Using a numerical model to understand the connection between the ocean and acoustic travel-time measurements. The Journal of the Acoustical Society of America, 134(4): 3211–3222, doi: 10.1121/1.4818786

Rainville L, Johnston T M S, Carter G S, et al. 2010. Interference pattern and propagation of the M2 internal tide south of the Hawaiian Ridge. Journal of Physical Oceanography, 40(2): 311–325, doi: 10.1175/2009JPO4256.1

Shang Xiaodong, Liu Qian, Xie Xiaohui, et al. 2015. Characteristics and seasonal variability of internal tides in the southern South China Sea. Deep Sea Research Part I: Oceanographic Research Papers, 98: 43–52, doi: 10.1016/j.dsr.2014.12.005

Tian Jiwei, Yang Qingxuan, Zhao Wei. 2009. Enhanced diapycnal mixing in the South China Sea. Journal of Physical Oceanography, 39(12): 3191–3203, doi: 10.1175/2009JPO3899.1

van Haren H. 2005. Tidal and near-inertial peak variations around the diurnal critical latitude. Geophysical Research Letters, 32(23): L23611, doi: 10.1029/2005GL024160

Xie Xiaohui, Liu Qian, Zhao Zhongxiang, et al. 2018. Deep sea currents driven by breaking internal tides on the continental slope. Geophysical Research Letters, 45(12): 6160–6166

Xie Xiaohui, Shang Xiaodong, Chen Guiying. 2010. Nonlinear interactions among internal tidal waves in the northeastern South China Sea. Chinese Journal of Oceanology and Limnology, 28(5): 996–1001, doi: 10.1007/s00343-010-9064-8

Xie Xiaohui, Shang Xiaodong, Van Haren H, et al. 2013. Observations of enhanced nonlinear instability in the surface reflection of internal tides. Geophysical Research Letters, 40(8): 1580–1586, doi: 10.1002/grl.50322

Xu Zhenhua, Liu Kun, Yin Baoshu, et al. 2016. Long-range propagation and associated variability of internal tides in the South China Sea. Journal of Geophysical Research: Oceans, 121(11): 8268–8286, doi: 10.1002/jgrc.v121.11

Xu Zhenhua, Yin Baoshu, Hou Yijun, et al. 2014. Seasonal variability and north-south asymmetry of internal tides in the deep basin west of the Luzon Strait. Journal of Marine Systems, 134: 101–112, doi: 10.1016/j.jmarsys.2014.03.002

Zhao Zhongxiang. 2014. Internal tide radiation from the Luzon Strait. Journal of Geophysical Research: Oceans, 119(8): 5434–5448, doi: 10.1002/2014JC010014

Zhao Zhongxiang, Alford M H, MacKinnon J A, et al. 2010. Long-range propagation of the semidiurnal internal tide from the Hawaiian Ridge. Journal of Physical Oceanography, 40(4): 713–736, doi: 10.1175/2009JPO4207.1